Nature Communications

https://doi.org/10.1038/s41467-026-69818-x

Article in Press

Global warming drives an increase in pre-monsoon tropical cyclone activity over the North Indian Ocean

Received: 4 May 2025

Accepted: 9 February 2026

Cite this article as: Shan, K., Song, F., Lin, Y. *et al.* Global warming drives an increase in pre-monsoon tropical cyclone activity over the North Indian Ocean. *Nat Commun* (2026). https://doi.org/10.1038/s41467-026-69818-x

Kaiyue Shan, Fengfei Song, Yanluan Lin, Pao-Shin Chu, Lixin Wu & Xiping Yu

Global warming drives an increase in pre-monsoon tropical cyclone activity over the North Indian Ocean

Kaiyue Shan[1], Fengfei Song[2,3], Yanluan Lin[4], Pao-Shin Chu[5], Lixin Wu[2,3], and Xiping Yu[6*]

1 State Key Laboratory of Hydroscience and Engineering, Department of Hydraulic Engineering, Tsinghua University, Beijing, China, 100084.

2 Frontier Science Center for Deep Ocean Multispheres and Earth System and Physical Oceanography Laboratory, Ocean University of China, Qingdao, China, 266100.

3 Laoshan Laboratory, Qingdao, China, 266100.

4 Department of Earth System Science, Ministry of Education Key Laboratory for Earth System Modeling, Institute for Global Change Studies, Tsinghua University, Beijing, China,100084.

5 Department of Atmospheric Sciences, School of Ocean and Earth Science and Technology, University of Hawai‘i at Mānoa, Honolulu, HI, USA, 96822.

6 Department of Ocean Science and Engineering, Southern University of Science and Technology, Shenzhen, China, 518055.

* Corresponding author:
Xiping Yu (yuxp@sustech.edu.cn)

Abstract

Early-season tropical cyclones (TCs), particularly in the pre-monsoon period (April–June) of the North Indian Ocean (NIO) basin, often cause exceptionally severe damage to populated landmasses despite being less frequent. A critical uncertainty is how these TCs respond to anthropogenic climate change. Here, we find a significant increasing trend in pre-monsoon TC activity in the NIO basin, with accumulated cyclone energy exhibiting a striking rise of 3.01×10^4 knots^2 per decade ($P < 0.05$) during 1981–2023, while the corresponding trend during the post-monsoon season (October–December) is weaker and insignificant. Climate models identify increased greenhouse gas as the primary driver, creating more favorable thermodynamic conditions for TC formation and maintenance in the NIO basin during the pre-monsoon season. These enhanced thermodynamic conditions are projected to intensify further, suggesting the increasing trend in pre-monsoon TC activity may continue to accelerate in the future.

Introduction

Early-season TCs are often less predictable[1-3], and their potential to bring heavy rainfall can lead to significant damage[1,4-7]. In the North Indian Ocean (NIO) basin, the early-season (April–June), also known as the pre-monsoon season, is characterized by TCs that pose a much higher risk. While the post-monsoon season (October–December) records more frequent TC occurrence, pre-monsoon TCs exhibit a statistically greater tendency to reach major intensity. Climatologically, about 26% of pre-monsoon TCs in the NIO basin intensify to Category 3 or stronger, compared to only 15% in the post-monsoon season[8]. This risk is clearly seen in some of the most devastating events. TC Nargis, a pre-monsoon event that struck Myanmar's Ayeyarwady River Delta in May 2008, brought exceptionally torrential rainfall, severe flooding, and devastating landslides, thereby precipitating the most catastrophic natural disaster in Myanmar's history, with a death toll exceeding 138,000[1,9]. The high fatalities caused by Nargis were closely linked to the lack of reliable forecasts and evacuation plans[10]. At the time, Nargis was the costliest and deadliest TC on record in the NIO basin, a record later broken by another pre-monsoon event, TC Amphan, in May 2020. Amphan caused widespread damage across Eastern India, incurring an economic toll exceeding $13 billion and establishing itself as the most expensive TC ever recorded in the NIO basin[11]. Given their devastating societal and economic impacts, there is a critical need to better understand how pre-monsoon TC activity in the NIO basin is changing under climate warming.

Despite their infrequent occurrence, pre-monsoon TCs in the NIO often lead to disproportionately severe impacts on densely populated coastal regions[8]. However, unlike other ocean basins, the sparse observational record and the more complex forcing–response relationship in the NIO basin make it particularly challenging to distinguish robust signals from background noise[12,13]. Consequently, it remains unclear whether any long-term changes in pre-monsoon TC activity over the NIO are detectable and to what extent such changes can be attributed to anthropogenic warming. In this study, we found a significant increase in pre-monsoon TC activity over the NIO basin, which is primarily driven by increasingly favorable thermodynamic conditions

under anthropogenic forcing. This work provides compelling observational evidence that anthropogenic warming is advancing the onset of the TC season[6], filling a critical gap in our understanding of how climate change influences TC seasonality across global ocean basins.

Results

Increasing trend in pre-monsoon TC activity

Here, we use accumulated cyclone energy (ACE)[14] to examine changes in pre-monsoon TC activity. Traditional frequency metrics are discrete and uncertain, especially in the NIO basin, where limited sample sizes further complicate the problem. By incorporating TC number, duration, and intensity, ACE overcomes these limitations and provides a more robust link to climate variables[15-18]. A significant increasing trend in the ACE of pre-monsoon (April–June) TCs in the NIO basin is observed, which drives the overall increase in annual TC ACE in this region. Figure 1a shows a significant increasing trend in annual TC ACE from 1981 to 2023 over the NIO basin at the 95% confidence level, with a rate of 4.98×10^4 knots^2 per decade. Notably, the pre-monsoon ACE emerges as a dominant driver of this long-term increasing trend, exhibiting a striking rise (3.01×10^4 knots^2 per decade) at the 95% confidence level (Figure 1c). In contrast, although both monsoon-season (July–September) and post-monsoon season (October–December) ACE show increasing trends, these changes are not statistically significant (Supplementary Figure 1). A parallel analysis of the power dissipation index (PDI)[19], another metric of TC activity, yields consistent results, reinforcing the seasonally asymmetric intensification pattern (Supplementary Figure 2).

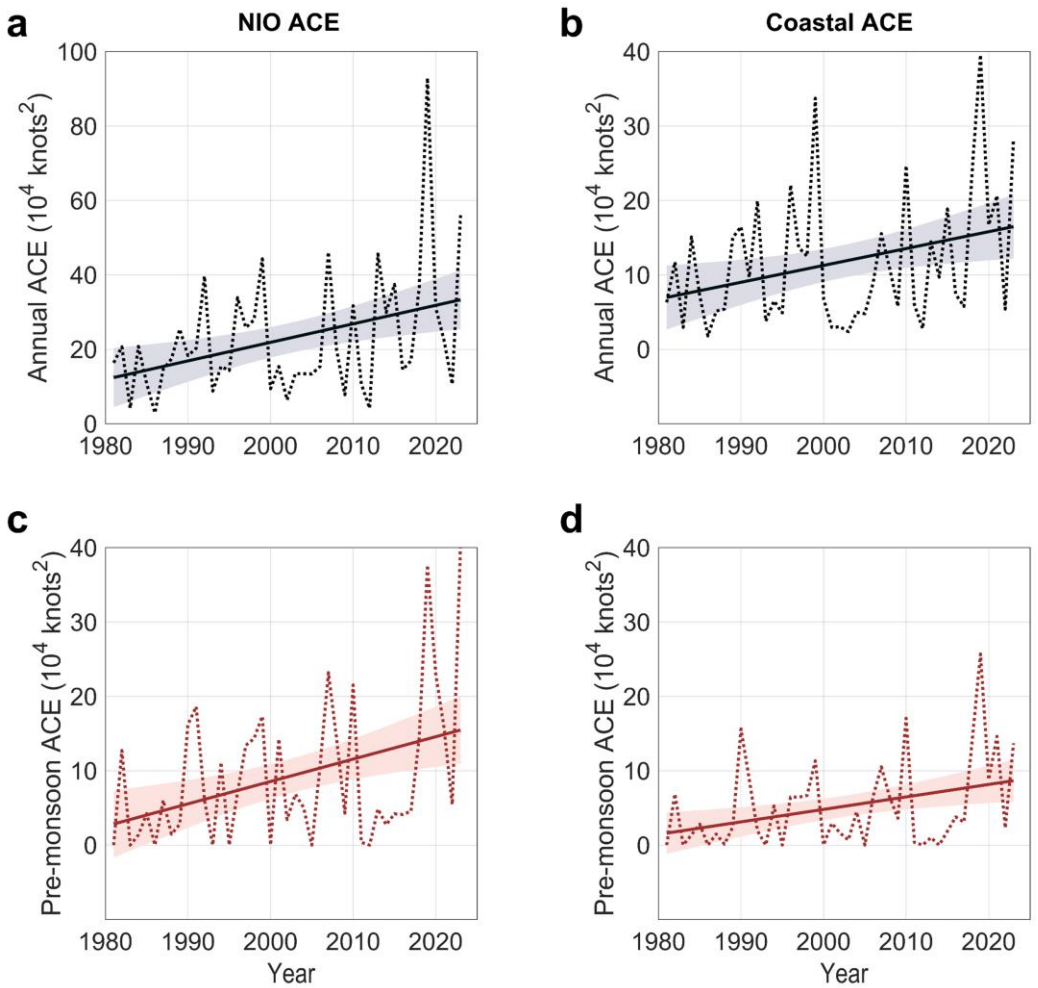

Figure 1 Increasing trends in accumulated cyclone energy (ACE) of the North Indian Ocean (NIO) basin. a-b, Time series of annual tropical cyclone (TC) ACE obtained from the best-track dataset from 1981 to 2023 (**a**) over the NIO basin, and (**b**) over the coastal areas of the NIO. **c-d,** Time series of TC ACE during the pre-monsoon season (April–June) from 1981 to 2023 (**c**) over the NIO basin, and (**d**) over the coastal areas of the NIO. Linear trends (solid lines) are significant at the 95% confidence level based on the Student's *t*-test. The shaded areas represent the 95% confidence intervals.

To ensure data quality, we analyze TC observations during the satellite era, when records are most complete and reliable across basins. We further assess the sensitivity of trend detection by varying the starting year while fixing the end year at 2023. The results indicate that the significantly increasing trends in both annual ACE and pre-monsoon ACE remain robust (Supplementary Figure 3). To evaluate the potential influence of the recent years with exceptionally high ACE, we recalculated the trends after excluding each of these years individually

(Supplementary Table 1). The increasing trends in both annual and pre-monsoon ACE remain statistically significant at the 95% confidence level in all cases, suggesting that our main finding is not driven by any single extreme year. Additionally, a change-point analysis detects no significant shift during the period 1981–2023 (Supplementary Figure 4), further supporting the reliability and robustness of the observed long-term trend. We also examine coastal ACE (Figures 1b, d), defined as the ACE within 300 km of the coastline. The result reveals significant increases in both annual and pre-monsoon ACE. Sensitivity tests using distance-to-land thresholds from 200 km to 500 km at 100-km intervals further confirm the robustness of these results (Supplementary Figure 5).

Figure 2 shows the spatial distribution of pre-monsoon TC activity over the NIO basin during the period 1981–2023. Although the climatological mean of pre-monsoon ACE is higher over the Bay of Bengal (BoB) than the Arabian Sea (AS), the rate of increase in pre-monsoon ACE is notably greater over the AS. Specifically, pre-monsoon ACE has increased by 39.5% (an absolute trend of 3.4×10^2 knots^2 per decade per grid point) in the AS, compared to 12.7% (2.0×10^2 knots^2 per decade per grid point) in the BoB. The AS exhibits an overall increase in pre-monsoon ACE between 65°E and 75°E. In the BoB, pre-monsoon ACE has increased primarily between 82.5°E and 90°E, whereas regions along the southern coasts of India and Bangladesh exhibit an insignificant decrease.

Next, it is essential to determine the extent to which the observed increase in ACE can be attributed to increased TC duration (quantified as annual TC days) or intensified TCs. Quantitative analysis indicates that longer annual TC durations in the pre-monsoon season are the primary driver of the increase in pre-monsoon ACE, with no significant influence from TC intensity (Supplementary Figure 6). Changes in annual TC durations follow the same striking seasonal pattern as in ACE, being pronounced in the pre-monsoon season but weak and statistically insignificant in the post-monsoon season. This seasonal divergence is clearly reflected in the spatial patterns of TC occurrence (Supplementary Figure 7). During the pre-monsoon season, TC frequency shows general increases across most of the NIO basin. In contrast, the post-monsoon

season displays a complex regional pattern, with increases over the western Arabian Sea offset by decreases across the eastern Arabian Sea and much of the BoB, which explains its weak basin-wide trend.

Regionally, during the pre-monsoon season, the increase in TC occurrence is more pronounced in the AS, with track density rising by 21.7% (an absolute increase of 0.42 per decade per grid point) in the AS and by only 1.1% (0.09 per decade per grid point) in the BoB (Figure 2d). A distinct west–east dipole pattern emerges across the BoB, where the density increases at west of 90°E but decreases at east of this longitude.

The role of thermodynamic conditions

Figure 2e shows the regressions of pre-monsoon ACE onto the genesis potential index (GPI)[20] within the region of highest TC activity in the NIO basin (10–20°N, 65–90°E). Enhanced pre-monsoon ACE over the AS is associated with higher GPI values, with regression coefficients ranging from $0.1 \sim 0.3 \times 10^4$ knots^2 per unit GPI. Over the BoB, the regression coefficients exhibit a zonal dipole pattern, which resembles the spatial pattern of TC occurrence changes shown in Figure 2d. A significant increasing trend in GPI over the NIO basin during the pre-monsoon season from 1981 to 2023 ($P < 0.05$) is observed (Figure 2f), indicating increasingly favorable environmental conditions for pre-monsoon TC activity.

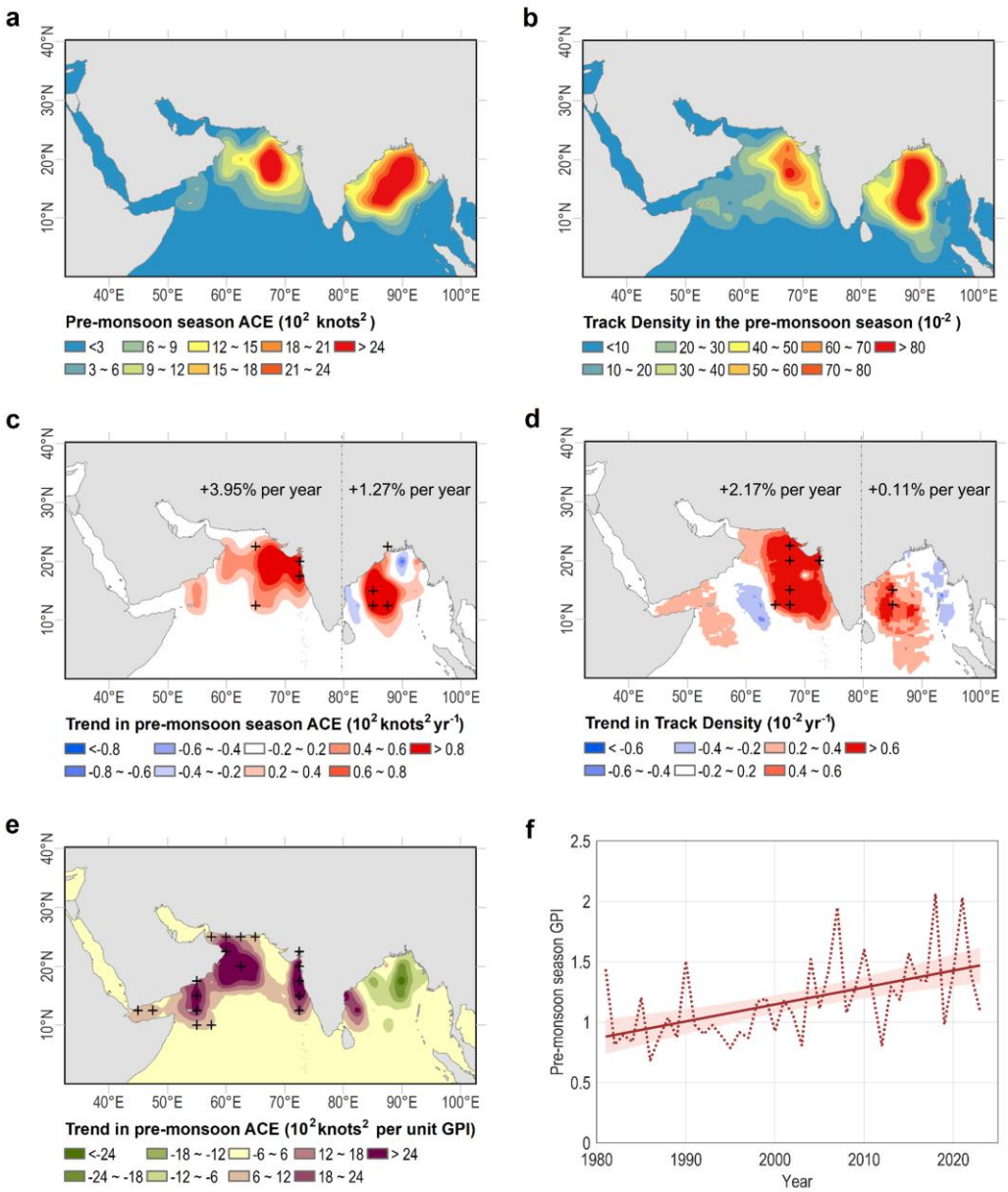

Figure 2 Connection between accumulated cyclone energy (ACE) and genesis potential index (GPI) during the pre-monsoon season. a-b, The spatial distributions of the (**a**) climatological mean of tropical cyclone (TC) ACE, and (b) TC track density obtained from the best-track dataset during the pre-monsoon season (April–June) over the North Indian Ocean (NIO) basin. **c-d,** Trends in (**c**) TC ACE, and (**d**) TC track density during the pre-monsoon season from 1981 to 2023. **e**, Regression trends in ACE per unit of GPI during the pre-monsoon season from 1981 to 2023. The black cross indicates the linear trend that is significant at the 95% confidence level. **f**, Time series of the mean value of GPI over the region 10–20°N, 65–90°E during the pre-monsoon season from 1981 to 2023. The linear trend (solid line) is significant at the 95% confidence level based on the Student's *t*-test. The shaded areas represent the 95% confidence intervals. The base map was generated using geographic coordinate system World Geodetic System 1984 generated by Global

Positioning System (maintained by the National Oceanic and Atmospheric Administration).

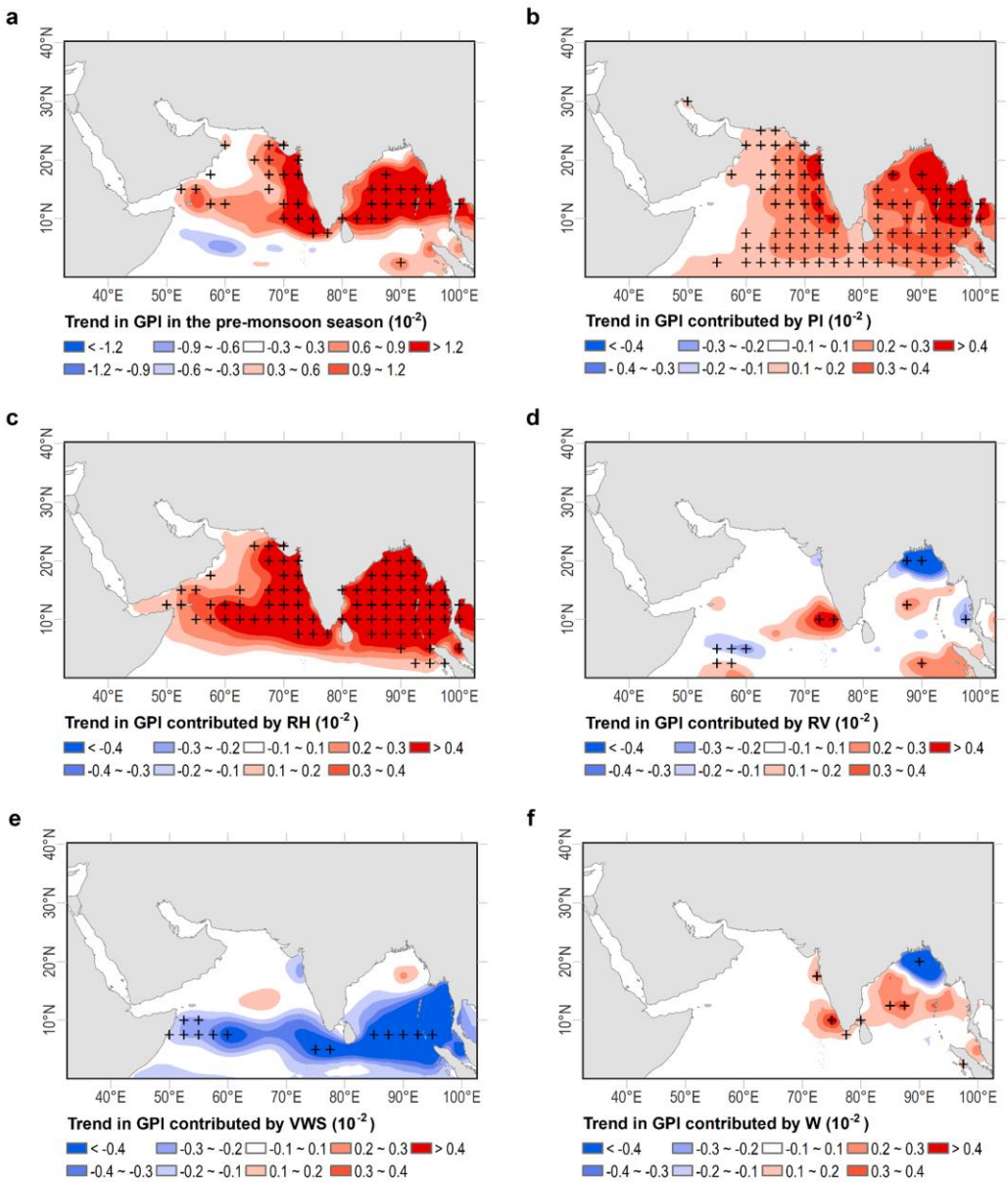

Figure 3 Trends in genesis potential index (GPI) during the pre-monsoon season and the contributions of environmental factors. a, Trends in GPI during the pre-monsoon season (April–June) over the North Indian Ocean (NIO) basin from 1981 to 2023. **b-f**, Trends in GPI during the pre-monsoon season for varying (**b**) potential intensity (PI), (**c**) relative humidity (RH), (**d**) relative vorticity (RV), (**e**) vertical wind shear (VWS), and (**f**) vertical wind velocity (W) with other environmental factors as climatology. The black cross indicates the linear trend that is significant at the 95% confidence level. The base map was generated using geographic coordinate system World Geodetic System 1984 generated by Global Positioning System (maintained by the National Oceanic and Atmospheric Administration).

The overall increasing trend in pre-monsoon GPI values results from changes in the individual thermodynamic and dynamic components of the index. The contributions of these environmental factors are evaluated separately (see Methods). As shown in Figure 3, the two thermodynamic components, i.e., potential intensity (PI) and relative humidity (RH), are the primary drivers of the increase in GPI over the NIO basin during the pre-monsoon season, while dynamic components contribute insignificantly.

While the basin-scale GPI trend roughly indicates increasingly favorable conditions (Figure 3a), we note that its empirical expressions may not fully capture all highly localized extremes. This appears to be the case in the northwestern Arabian Sea, where a very strong increase in ACE (Figure 2c) is not matched by a proportionally large GPI trend. Decomposition of the GPI into its individual physical components (Supplementary Figure 7) reveals that, in this specific region, the key thermodynamic factors (PI and RH) exhibit pronounced upward trends, while the dynamic factors remained relatively stable or slightly favorable. This analysis reaffirms that thermodynamic changes are the principal driver of increased TC activity, even in cases where the integrated GPI index may underrepresent sub-regional extremes.

Thermodynamic dominance is also evident when the contrasting environmental configurations between different seasons are paid attention. During the pre-monsoon season, PI increases across almost the entire NIO basin, providing widespread thermodynamic support. In contrast, the post-monsoon season lacks such a basin-wide increase in PI. Specifically, in the northern Bay of Bengal, a decrease in PI largely offsets the otherwise favorable influences from increasing humidity and improved dynamic conditions. Meanwhile, in the low-latitude Bay of Bengal, although both PI and RH increase, these thermodynamic supports are offset by enhanced VWS, resulting in a net environment unfavorable to TC genesis and development (Supplementary Figure 7). This fact contributes to the observed differences in TC activity trends between the two seasons.

To quantify the relative influences of anthropogenic and natural forcings on the enhanced thermodynamic factors in the NIO basin, we analyzed the individual contributions of greenhouse

gases, natural forcings, and anthropogenic aerosols using historical single-forcing simulations from the Detection and Attribution Model Intercomparison Project (DAMIP) within CMIP6 (see Methods). As shown in Figure 4, the observed increasing trends in PI and RH during the pre-monsoon season are predominantly driven by greenhouse gas (GHG) forcing. Factor separation analysis indicates that the rise in PI is largely attributable to the increase in sea surface temperature (Supplementary Figure 8). Correspondingly, GHG forcing is also identified as the dominant driver of the concurrent sea surface temperature increase, establishing a coherent mechanistic pathway. In contrast, anthropogenic aerosols (AER) exert a suppressing effect, partially offsetting the GHG-induced increases, while the contribution from natural forcing (NAT) is negligible. This attribution analysis is robust to the geographical boundaries of the analysis domain (Supplementary Figure 9).

To further corroborate these findings, we examined future projections of PI and RH over the period 2015–2099 under the SSP5-8.5 scenario. Both PI and RH exhibit significant upward trends, with 95% confidence intervals indicated in parentheses (Figure 4), suggesting a continued intensification of thermodynamic conditions favorable for TC activity in the NIO basin during the pre-monsoon season.

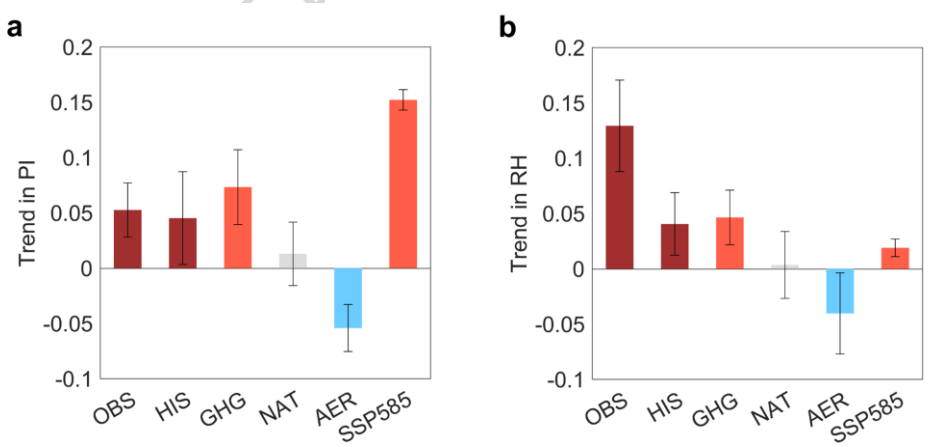

Figure 4 Observed and simulated trends in thermodynamic factors during the pre-monsoon season. Trends in (**a**) potential intensity (PI), and (**b**) relative humidity (RH) during the pre-monsoon season (April–June). The analysis domain is 10–20°N, 65–90°E. Observed results (OBS) obtained from the ECMWF and ERA-5 datasets from 1981 to 2023, results from the multimodel mean of CMIP6 historical (HIS) simulations, results from the multimodel mean of simulations forced by greenhouse gas (GHG) only, natural forcing (NAT) only and anthropogenic aerosol (AER) only based on the Detection and Attribution Model Intercomparison Project from 1981 to

2014, and results from the multimodel mean of the future high-emission scenario (Shared Socioeconomic Pathway 585; SSP585) simulations from 2015 to 2099 are shown. Linear trends (bars) are significant at the 95% confidence level based on the Student's *t*-test. The error bars indicate the 95% confidence intervals.

Discussion

In summary, our observational analysis reveals a significantly increasing trend in the ACE of TCs over the NIO basin during the pre-monsoon season, which substantially contributes to the overall rise in annual TC ACE in this region. In contrast, the trend during the post-monsoon season is much weaker and statistically insignificant. We have further examined the environmental factors to clarify why TC activity has increased specifically in the pre-monsoon season. The rise in ACE is driven mainly by more frequent TC occurrence, and not by strengthened intensity. During the pre-monsoon season, TC occurrence increases across most of the NIO, while in the post-monsoon season, the variation pattern is more complex, with increases over the western Arabian Sea and decreases in the Bay of Bengal. This seasonal difference arises because the pre-monsoon season benefits from strong and widespread enhancement of thermodynamic conditions across the whole NIO basin, whereas thermodynamic support in the post-monsoon season is weaker and more regionally dependent.

The enhancement of thermodynamic conditions during the pre-monsoon season is projected to intensify under future emission scenarios, indicating that the upward trend in pre-monsoon TC activity over the NIO basin is likely to persist. Given the high population density and vulnerability of the coastal regions surrounding the NIO basin, such changes have profound implications for regional disaster preparedness, early-warning systems, and long-term adaptation strategies. From a broader perspective, these findings provide an additional key piece of observational evidence supporting the conclusion that global warming is amplifying early-season TC activity worldwide. This highlights the urgent need to reassess current risk management frameworks and integrate the growing hazard of pre-monsoon TCs into future climate resilience planning.

Methods

TC data

TC data are obtained from the International Best-Track Archive for Climate Stewardship version 4[13] for the period of 1981–2023. In particular, we use the best-track records from the Joint Typhoon Warning Center (JTWC), as archived in IBTrACS. The JTWC provides a continuous satellite-era record since 1972, and its reliability for the NIO after the 1980s is well known [21-23]. A key data concern in the NIO prior to 1990 is its involving the India Meteorological Department (IMD) records, which lack TC intensity estimates during this early period[24]. To ensure a homogeneous record essential for detecting long-term trends, we use the original JTWC records for position and intensity, rather than multi-agency estimates. This approach addresses known inter-agency inconsistencies, as quantified by Kabir et al. (ref. 25) in their valuable work to reconcile systematic biases and create a more complete record. For our specific focus on trend detection, maintaining temporal consistency within a single, consistently processed dataset avoids introducing spurious inhomogeneities that could arise from merging different sources[23, 24].

Our analysis is based on a total of 228 NIO TCs over the period 1981–2023, with the seasonal distribution of approximately 30% in the pre-monsoon, 10% in the monsoon, and 60% in the post-monsoon season.

TC activity metrics

Given the relatively low sample size in the NIO basin, we employ the accumulated cyclone energy (ACE) index[14] as our primary metric of TC activity. ACE integrates duration and intensity information for each individual TC, providing a more robust measure of overall activity than TC frequency alone, particularly in basins with fewer events. For each TC (i), the ACE_i is calculated as follows:

$$ACE_i = \sum_{0}^{\tau} V_{\max}^2 \quad (1)$$

where $V_{\max}$ is the maximum sustained surface wind speed at each 6-hourly time interval over the TC duration (τ). The ACE of a specific ocean basin is the summation of all TC events (n) passing that region, which is calculated as follows:

$$ACE = \sum_{1}^{n} \sum_{0}^{\tau} V_{\max}^2 \quad (2)$$

Similar to the ACE, the PDI[19] of a specific ocean basin or worldwide can be calculated as follows:

$$PDI = \sum_{1}^{n} \sum_{0}^{\tau} V_{\max}^3 \quad (3)$$

Generation of spatial maps

Spatial maps of TC metrics were derived from data calculated on a 2.5° × 2.5° grid. A given TC is counted only once in a particular unit area. This resolution was chosen to retain relevant spatial details while maintaining sufficient sample counts per grid for statistical robustness. A sensitivity analysis confirmed that the key spatial patterns were robust to the choice of grid resolution. To produce continuous fields from these discrete grid values, we applied Empirical Bayesian Kriging interpolation. This method smooths the data while preserving large-scale spatial patterns, reducing the visual influence of individual grid cells with low sample counts.

GPI

To connect TC activity to environmental changes, we employ the genesis potential index (GPI)[20], a composite metric that reflects the combined influence of thermodynamic and dynamic factors on TC genesis and development, which is expressed as

$$GPI = \left|10^5 \eta\right|^{3/2} \left(\frac{RH}{50}\right)^3 \left(\frac{PI}{70}\right)^3 \left(1+0.1VWS\right)^{-2} \left(\frac{-W+0.1}{0.1}\right) \quad (4)$$

where η is the absolute vorticity at 850 hPa (/s), *RH* is the relative humidity at 700 hPa (%), *PI* is the potential intensity (in terms of maximum wind; m/s), *VWS* is the vertical wind shear between the horizontal winds at 200 hPa and 850 hPa (m/s), and *W* is the vertical wind velocity (Pa/s). In our study, the GPI was calculated using environmental variables from the ERA5 reanalysis[26].

The relative importance of each environmental factor is evaluated by computing GPI anomalies in sensitivity experiments, where one factor is set to its value during the active period while the other four are held at their climatological means[27].

To quantify the statistical relationship between TC activity and environmental factors, we performed linear regression of ACE onto the GPI index across the core NIO region (10°–20°N, 65°–90°E). The GPI was used as it integrates key thermodynamic and dynamic parameters governing TC genesis and development. The regression coefficient at each grid point thus represents the change in ACE per unit change in this composite environmental index. The regression coefficient at each grid point represents the change in ACE per unit change in GPI.

CMIP6 models

To assess the relative contributions of anthropogenic and natural forcings, we utilize all available simulations from the Detection and Attribution Model Intercomparison Project (DAMIP) within CMIP6 (Supplementary Table 2)[28-36]. DAMIP is specifically designed to quantify the individual impacts of anthropogenic and natural forcings on observed global and regional climate changes. The historical single-forcing experiments include: (1) hist-GHG, which isolates the effects of greenhouse gases; (2) hist-nat, which incorporates only natural forcings such as solar variability and volcanic aerosols; and (3) hist-aer, which includes only anthropogenic aerosols. To examine projected changes over the twenty-first century, we further analyze simulations conducted under the SSP5-8.5 emissions scenario using the same set of models.

The domain for analysis is 10°N–20°N, 65°E–90°E, covering the main region of TC activity in the NIO. To ensure that our attribution analyses were robust to the specific geographical boundaries, we conducted a sensitivity analysis by calculating trends over two additional domains: a larger region (5°N–25°N, 50°E–100°E) and a smaller region (10°N–20°N, 70°E–85°E). The results obtained over these different domains are presented in Supplementary Figure 9.

Data availability

TC data are obtained from the IBTrACS (https://www.ncei.noaa.gov/products/international-best-track-archive). The ERA-5 reanalysis data are available at https://cds.climate.copernicus.eu/datasets/reanalysis-era5-single-levels-monthly-means?tab=overview. The raw outputs of CMIP6 models are available at available at https://esgf-node.llnl.gov/search/cmip6/.

Code Availability

Code for figure plotting can be obtained at https://zenodo.org/records/18477970.

References

1. Fritz, H., Blount, C., Thwin, S. et al. Cyclone Nargis storm surge in Myanmar. Nat. Geosci. 2, 448–449 (2009).
2. Elsberry, R. L., Jordan, M. S. & Vitart, F. Predictability of tropical cyclone events on intraseasonal timescales with the ECMWF monthly forecast model. Asia-Pac. J. Atmos. Sci. 46, 135–153 (2010).
3. Wang, C., Wang, B. & Wu, L. Abrupt breakdown of the predictability of early season typhoon frequency at the beginning of the twenty-first century. Clim. Dyn. 52, 3809–3822 (2019).

4. Truchelut, R. E., Klotzbach, P. J., Staehling, E. M. et al. Earlier onset of North Atlantic hurricane season with warming oceans. Nat. Commun. 13, 4646 (2022).

5. Fan, X., Li, Y. & Liu, Y. Characteristics of precipitation in China associated with tropical cyclones over the Bay of Bengal. J. Meteorol. Res. 37, 417–430 (2023).

6. Shan, K., Lin, Y., Chu, P.-S. et al. Seasonal advance of intense tropical cyclones in a warming climate. Nature 623, 83–89 (2023).

7. Ranjan, R. & Karmakar, S. Compound hazard mapping for tropical cyclone-induced concurrent wind and rainfall extremes over India. npj Nat. Hazards 1, 15 (2024).

8. Singh, V. K. & Roxy, M. K. A review of ocean-atmosphere interactions during tropical cyclones in the north Indian Ocean. Earth-Sci. Rev. 226, 103967 (2022).

9. Li, W. W., Wang, C., Wang, D. et al. Modulation of low-latitude west wind on abnormal track and intensity of tropical cyclone Nargis (2008) in the Bay of Bengal. Adv. Atmos. Sci. 29, 407–421 (2012).

10. Lin, N. & Emanuel, K. Grey swan tropical cyclones. Nat. Clim. Change 6, 106–111 (2016).

11. Nandakumar, P., Chakravarty, K., Jana, D., Kannan, B. A. M., Siddiqui, J. Y. & Paul, A. Features of atmospheric dynamics during tropical cyclone AMPHAN observed using ST radar and Doppler weather radar. IEEE Trans. Geosci. Remote Sens. 62, 5105208 (2024).

12. Kossin, J. P., Olander, T. L. & Knapp, K. R. Trend analysis with a new global record of tropical cyclone intensity. J. Clim. 26, 9960–9976 (2013).

13. Knapp, K. R. et al. The International Best Track Archive for Climate Stewardship (IBTrACS): Unifying tropical cyclone data. Bull. Am. Meteorol. Soc. 91, 363–376 (2010).

14. Bell, G. D., Halpert, M. S., Schnell, R. C., Higgins, R. W., Lawrimore, J., Kousky, V. E., Tinker, R., Thiaw, W., Chelliah, M. & Artusa, A. Climate assessment for 1999. Bull. Am. Meteorol. Soc. 81, S1–S50 (2000).

15. Maue, R. N. Recent historically low global tropical cyclone activity. Geophys. Res. Lett. 38, L14803 (2011).

16. Lin, I.-I. & Chan, J. C. L. Recent decrease in typhoon destructive potential and global warming

implications. Nat. Commun. 6, 7182 (2015).

17. EPA (Environmental Protection Agency of United States). Climate change indicators: tropical cyclone activity (2016).
18. Shan, K. et al. How does globally accumulated tropical cyclone energy vary in response to a changing climate? Sci. Bull. 70, 943–950 (2025).
19. Emanuel, K. Increasing destructiveness of tropical cyclones over the past 30 years. Nature 436, 686–688 (2005).
20. Murakami, H. & Wang, B. Future change of North Atlantic tropical cyclone tracks: projection by a 20-km-mesh global atmospheric model. J. Clim. 23, 2699–2721 (2010).
21. Chu, J-H. Sampson, C. R. Levine, A. S. & Fukada, E. The Joint Typhoon Warning Center tropical cyclone best-tracks, 1945–2000. U.S. Naval Research Laboratory Rep. NRL/MR/7540-02-16, 22 pp (2002).
22. Singh, O. P. Recent Trends in Tropical Cyclone Activity in the North Indian Ocean. Indian Ocean Tropical Cyclone and Climate Change. Springer Dordrecht Heidelberg London New York. 51 pp (2010).
23. Evan, A. T. & Camargo, S. J. A Climatology of Arabian Sea Cyclonic Storms. Journal of Climate, 24, 140-158 (2011).
24. Knapp, K. R., & Kruk, M. C. Quantifying Interagency Differences in Tropical Cyclone Best-Track Wind Speed Estimates. Mon. Wea. Rev., 138, 1459–14731 (2010).
25. Kabir, R. Ritchie, E. A. & Stark, C. Tropical Cyclone Exposure in the North Indian Ocean. Atmosphere, 13, 1421 (2022).
26. Hersbach, H., et al. The ERA5 global reanalysis. Quart. J. R. Met. Soc. 146, 1999–2049 (2020).
27. Camargo, S., Emanuel, K. & Sobel, A. Use of a genesis potential index to diagnose ENSO effects on tropical cyclone genesis. J. Clim. 20, 4819–4834 (2007).
28. Bi, D. et al. Configuration and spin-up of ACCESS-CM2, the new generation Australian Community Climate and Earth System Simulator Coupled Model. J. South. Hemis. Earth Syst. Sci. (2020).

29. Wu, T. et al. Beijing Climate Center Earth System Model version 1 (BCC-ESM1): model description and evaluation of aerosol simulations. Geosci. Model Dev. 13, 977–1005 (2020).
30. Swart, N. C. et al. The Canadian Earth System Model version 5 (CanESM5.0.3). Geosci. Model Dev. 12, 4823–4873 (2019)..
31. Danabasoglu, G. et al. The Community Earth System Model Version 2 (CESM2). J. Adv. Model. Earth Syst. 12, e2019MS001916 (2020).
32. Li, L. et al. The flexible global ocean–atmosphere–land system model grid-point version 3 (FGOALS-g3): description and evaluation. J. Adv. Model. Earth Syst. 12, e2019MS002012 (2020).
33. Kelley, M. et al. GISS-E2.1: Configurations and climatology. J. Adv. Model. Earth Syst. 12, e2019MS002025 (2020).
34. Boucher, O. et al. Presentation and evaluation of the IPSL-CM6A-LR climate model. J. Adv. Model. Earth Syst. 12, e2019MS002010 (2020).
35. Yukimoto, S., Kawai, H., Koshiro, T. et al. The Meteorological Research Institute Earth System Model version 2.0, MRI-ESM2.0: Description and basic evaluation of the physical component. J. Meteorol. Soc. Jpn. 97, 931–965 (2019).
36. Seland, Ø., Bentsen, M., Olivié, D. et al. Overview of the Norwegian Earth System Model (NorESM2) and key climate response of CMIP6 DECK, historical, and scenario simulations. Geosci. Model Dev. 13, 6165–6200 (2020).

Acknowledgements

This research is supported by the Young Elite Scientists Sponsorship Program by China Association for Science and Technology under grants No. 2023QNRC001 (Kaiyue Shan), and National Natural Science Foundation of China (NSFC) under grants No. 41961144014 (Xiping Yu) and No. 42175029 (Fengfei Song).

Author Contributions Statement

K. S. and X. Y. designed the research. K. S. performed the analysis, drew all the figures and wrote the first draft of the paper. K.S., F. S., Y. L., P.-S. C., L.W., and X. Y. provided comments on different versions of the paper.

Competing Interests Statement

The authors declare that they have no conflict of interest.

Figure Legends

Figure 1 Increasing trends in accumulated cyclone energy (ACE) of the North Indian Ocean (NIO) basin. a-b, Time series of annual tropical cyclone (TC) ACE obtained from the best-track dataset from 1981 to 2023 (**a**) over the NIO basin, and (**b**) over the coastal areas of the NIO. **c-d,** Time series of TC ACE during the pre-monsoon season (April–June) from 1981 to 2023 (**c**) over the NIO basin, and (**d**) over the coastal areas of the NIO. Linear trends (solid lines) are significant at the 95% confidence level based on the Student's *t*-test. The shaded areas represent the 95% confidence intervals.

Figure 2 Connection between accumulated cyclone energy (ACE) and genesis potential index (GPI) during the pre-monsoon season. a-b, The spatial distributions of the (**a**) climatological mean of tropical cyclone (TC) ACE, and (b) TC track density obtained from the best-track dataset during the pre-monsoon season (April–June) over the North Indian Ocean (NIO) basin. **c-d,** Trends in (**c**) TC ACE, and (**d**) TC track density during the pre-monsoon season from 1981 to 2023. **e**, Regression trends in ACE per unit of GPI during the pre-monsoon season from 1981 to 2023. The black cross indicates the linear trend that is significant at the 95% confidence level. **f**, Time series of the mean value of GPI over the region 10–20°N, 65–90°E during the pre-monsoon season from 1981 to 2023. The linear trend (solid line) is significant at the 95% confidence level based on the Student's *t*-test. The shaded areas represent the 95% confidence intervals. The base map was generated using geographic coordinate system World Geodetic System 1984 generated by Global Positioning System (maintained by the National Oceanic and Atmospheric Administration).

Figure 3 Trends in genesis potential index (GPI) during the pre-monsoon season and the contributions of environmental factors. a, Trends in GPI during the pre-monsoon season (April–

June) over the North Indian Ocean (NIO) basin from 1981 to 2023. **b-f**, Trends in GPI during the pre-monsoon season for varying (**b**) potential intensity (PI), (**c**) relative humidity (RH), (**d**) relative vorticity (RV), (**e**) vertical wind shear (VWS), and (**f**) vertical wind velocity (W) with other environmental factors as climatology. The black cross indicates the linear trend that is significant at the 95% confidence level. The base map was generated using geographic coordinate system World Geodetic System 1984 generated by Global Positioning System (maintained by the National Oceanic and Atmospheric Administration).

Figure 4 Observed and simulated trends in thermodynamic factors during the pre-monsoon season. Trends in (**a**) potential intensity (PI), and (**b**) relative humidity (RH) during the pre-monsoon season (April–June). The analysis domain is 10–20°N, 65–90°E. Observed results (OBS) obtained from the ECMWF and ERA-5 datasets from 1981 to 2023, results from the multimodel mean of CMIP6 historical (HIS) simulations, results from the multimodel mean of simulations forced by greenhouse gas (GHG) only, natural forcing (NAT) only and anthropogenic aerosol (AER) only based on the Detection and Attribution Model Intercomparison Project from 1981 to 2014, and results from the multimodel mean of the future high-emission scenario (Shared Socioeconomic Pathway 585; SSP585) simulations from 2015 to 2099 are shown. Linear trends (bars) are significant at the 95% confidence level based on the Student's *t*-test. The error bars indicate the 95% confidence intervals.

Editorial summary: Pre-monsoon tropical cyclones are particularly devastating in the North Indian Ocean. Global warming is increasing their activity, a trend likely to continue and raise risks for vulnerable coastal communities.

Peer review information: *Nature Communications* thanks the anonymous reviewer(s) for their contribution to the peer review of this work. A peer review file is available.